Graphical Abstract

Correlating Dimensionless Enthalpy, Pyrometry, and Melt Pool Geometry Within the Laser Powder Bed Fusion Energetic Regime: A Path to In-Situ Melt Pool Control Demonstrated on Tungsten.

Janko Stajkovic,Manuel Kahl,Lukas Kaserer,Jakob Braun,Sophie Scheuringer,Bernhard Mayr-Schmölzer,Benedikt Distl,Gerhard Leichtfried

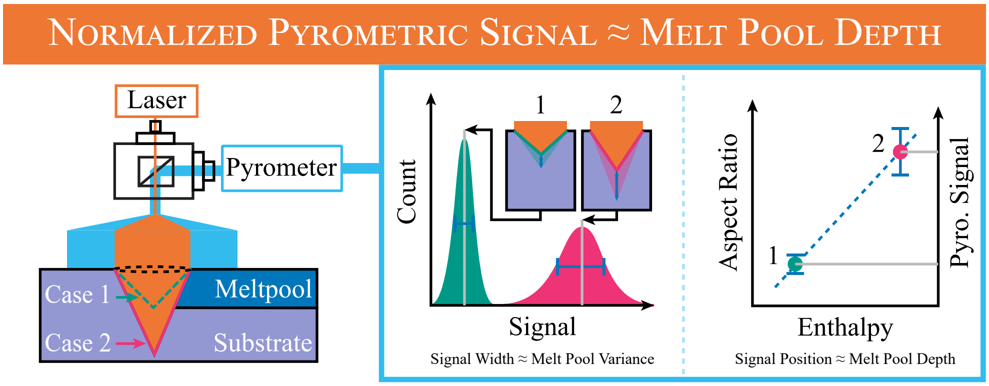

Highlights

Correlating Dimensionless Enthalpy, Pyrometry, and Melt Pool Geometry Within the Laser Powder Bed Fusion Energetic Regime: A Path to In-Situ Melt Pool Control Demonstrated on Tungsten.

Janko Stajkovic,Manuel Kahl,Lukas Kaserer,Jakob Braun,Sophie Scheuringer,Bernhard Mayr-Schmölzer,Benedikt Distl,Gerhard Leichtfried

- Pyrometer signal normalized by the spot size squared scales linearly to dimensionless enthalpy
- Pyrometric signal is mainly influenced by the depth of the keyhole
- Histographic signatures of pyrometric data correlate to keyhole stability and melting mode
- Enthalpy models can be used to predict the aspect ratio of a single line

Correlating Dimensionless Enthalpy, Pyrometry, and Melt Pool Geometry Within the Laser Powder Bed Fusion Energetic Regime: A Path to In-Situ Melt Pool Control Demonstrated on Tungsten.

Janko Stajkovic[a,*], Manuel Kahl[a], Lukas Kaserer[a], Jakob Braun[a], Sophie Scheuringer[a], Bernhard Mayr-Schmölzer[b], Benedikt Distl[b] and Gerhard Leichtfried[a]

[a]*Faculty of Engineering Sciences, Department of Mechatronics, Materials Science, Universität Innsbruck, Innrain 52, Innsbruck 6020, Austria*
[b]*Plansee SE, Metallwerk-Plansee-Straße 71, Reutte 6600, Austria*

ARTICLE INFO

Keywords:
LPBF
Pyrometry
Dimensionless enthalpy
Tungsten

ABSTRACT

In the realm of laser powder bed fusion (LPBF), controlling the melt pool in situ represents a critical challenge, as numerous defects are associated with its dynamics. This research demonstrates the utility of pyrometric signals in gaining insights into the depth of vapor capillaries during LPBF processes. By establishing a correlation between a semi-empirical enthalpy model and pyrometric data, gathered on a powder-free substrate, a pathway towards the in-situ control of melt pool geometry is unveiled. The study introduces a dimensionless enthalpy model designed for predicting the aspect ratio of melt pools in LPBF. A linear relationship between the depth of melt pools, pyrometric signals, and dimensionless enthalpy is established through correlation with this model and measurements from metallographic cross sections. Histographic analysis of pyrometric data reveals unique signatures that correlate with conduction and keyhole mode melting, suggesting that these distinct histogram forms are indicative of keyhole stability. The findings confirm that the relationships defined in this study are applicable across varying spot sizes and hatch distances, allowing for the inference of optimal parameters directly from pyrometric signals. This research lays the groundwork for real-time control of melt pool geometry, marking a significant advancement towards enhancing the quality and consistency of LPBF and holds potential applications to laser welding processes.

1. Introduction

The geometry of a melt pool, created by a single laser scan in the Laser Powder Bed Fusion (LPBF) process [1], serves as the cornerstone of the entire manufacturing mechanism, much like the role of the foundation in supporting and shaping the structure of a building. Just as the strength, stability and integrity of a building, depend on its foundation, the success and quality of LPBF-produced components rely among other process parameters on the precise control and understanding of melt pool geometry. In LPBF, a part is created by arranging a myriad of single hatch lines next to and on top of each other [1]. Contemporary LPBF parts are riddled with defects, some of which can be traced back to the specific melt pool geometries [2].

It has been observed that primary laser parameters, including laser power, speed, and spot size, when set to levels that result in low energy input, can lead to the formation of lack of fusion pores [3, 4][1]. Under these conditions, the cross section of the melt pool is typically semicircular, characterized by minimal to no vaporization. The majority of

*Corresponding author
janko.stajkovic@uibk.ac.at (J. Stajkovic)
ORCID(s): 0000-0002-7799-4846 (J. Stajkovic)

[1]Note that lack of fusion pores do not exclusively form due to low energy input. Other parameters, such as the choice of an adverse hatch distance, can yield an increase in lack of fusion porosity [5]

the laser energy in such scenarios is dissipated through thermal conduction, leading to the classification of this process regime as conduction mode.

In contrast, when laser parameters are adjusted to high energy levels, significant vaporization occurs. This process generates a recoil pressure that displaces molten material laterally, facilitating a drilling effect by the laser and resulting in the formation of a vapor depression [6, 7]. The depth of the vapor depression often surpasses its width due to multiple reflections within the depression [6, 8–11], leading to a cross sectional geometry akin to keyholes. This phenomenon is known as keyhole mode melting or keyholing. In this case, the energy input by the laser exceeds what can be dissipated through thermal conduction alone. Instead, convective melt pool flows, spurred by the vaporization, predominantly contribute to energy dissipation. Defects characteristic of this regime include keyhole pores [10, 12–14], which are remnants of keyhole collapse [11, 13], and centerline cracks [15], which arise from thermal stresses during solidification.

Located between these two melting modes is a parameter region that induces the minimal number of defects [12, 16]. This region is characterized by the formation of a keyhole through vaporization and recoil pressure, yet, unlike in laser-welding, its depth and width remain similar in size (consider the keyhole geometries observed by Cunningham et al. [17]). The goal is to operate within this regime to minimize defects, though achieving this necessitates comprehensive experimentation for each LPBF machine and material combination. Various models [8, 16, 18–20] have been developed to characterize this region, thereby aiming to lessen the experimental efforts required to identify optimal parameters.

Moreover, incorporating rapidly changing, local conditions during the LPBF process into these models is, at best, an approximation. Local conditions, such as heat accumulation at hatches in corners and overhang situations, can theoretically be addressed by some of the aforementioned models through adjustments in initial temperature or heat conductivity [20, 21]. However, for complex parts, it becomes unrealistic to accurately describe local conditions at every point in the build. The local environment in which a single hatch line is produced during LPBF can have an impact on the melt pool geometry that is as significant as the primary laser parameters chosen [22, 23]. The search for parameters that result in minimal defects thus becomes a daunting task, requiring exhaustive experimentation for each conceivable geometry. Given that a major advantage of using LPBF is the manufacturing of complex parts (e.g., near-net shape, embedded cooling channels, gyroids, etc.), relying solely on such models in the quest for defect-free parts appears to be only part of the solution.

The solution to numerous problems outlined above is conceptually simple to articulate yet challenging to implement. The objective would be to monitor the melt pool geometry and maintain it at an optimal level previously identified. It comes as no surprise that a segment of the scientific community, including the work presented here, is endeavoring to develop methods to achieve this [24].

High-speed optical imaging stands as one of the primary tools for investigating process dynamics in LPBF [24]. Numerous studies have shown the intricate dynamics present in LPBF: Scipioni Bertoli et al. [25] have illustrated that the laser primarily interacts with molten material. Ly et al. [26] identified the key factors in spatter generation, highlighting the effect of vapor induced powder particle entrainment, during LPBF. Bidare et al. [27, 28] employed high-speed imaging alongside a schlieren imaging setup to reveal the intricate interactions between the atmosphere, plume, and metal vapor, as well as spatter generation. It is clear that the length and width of the melt pool can be measured using top-down images from high-speed cameras. The depth of the melt pool could be inferred from the angle of the vapor plume, or the front wall angle [17, 26], although this necessitates complex image analysis. To the authors best knowledge, no publication to date has explored in-situ control of the melt pool using data gathered from high-speed optical imaging. Access to the depth of a melt pool remains challenging through these means.

In the studies referenced [13, 17, 29–34], x-rays were employed to in-situ capture the dynamics of melt pool formation. Cunningham et al. [17] showed that a transition region between keyhole and conduction mode can be defined. Simonds et al. [32, 33] demonstrated that the absorption of laser energy correlates with the geometry of the keyhole. Hamidi Nasab et al. [13] found that acoustic emission signals have a proportional relationship with the keyhole geometry. Khairallah et al. [35] indicated that periodic oscillations in the keyhole geometry precede the generation of keyhole pores, and described the generation of keyhole pores with high fidelity. While this list is not exhaustive, the effectiveness of x-ray imaging in revealing the complexities of melt pool and keyhole formation is clear. However, such setups require specialized, laboratory-scale equipment. The adaptation of these techniques for use on industrial machines appears unfeasible, and developing a viable concept for a feedback mechanism to respond to rapid in-situ changes seems impractical.

Compared to the previously discussed methods of monitoring the melt pool, pyrometric data collection is somewhat exotic, given the limited number of publications on the subject [24]. Lane et al. [36] showed that the intensity signal from a photodiode correlates with the absorptance of a melt pool. Further, it was hypothesized that the photodiode signal might also relate to the surface morphology of the melt pool, a plausible hypothesis considering that Simonds et al. [33] found a correlation between absorptance and melt pool geometry. Forien et al. [12], in efforts to detect keyhole pores via pyrometric signals, demonstrated that histographic analysis leads to distinct signatures for conduction, transition, and keyhole mode melting. Further, a correlation between pyrometric signals and melt pool depth was shown. Empirically, Vallabh et al. [37] utilized pyrometric data to train a support vector machine that successfully predicts the depth of a melt pool to a reasonable degree. In an experiment aimed at synthesizing oxides in-situ in stainless steel, Haines et al. [38] also concluded that the pyrometer is primarily sensitive to melt pool geometry. Unlike other measurement methods mentioned earlier, Renken et al. [39] proved that in-process measurement and closed-loop control using pyrometric data are feasible. Moreover, such a closed-loop control system based on these findings is currently commercially available, with a feedback time of 22 µs [40].

Given the evidence outlined previously, the development of a method for controlling melt pool geometry in-situ appears feasible using pyrometric data. There is accumulating evidence supporting the correlation between pyrometric signals and melt pool geometry. However, to date, no study has specifically focused on describing and explaining this correlation in detail.

This paper addresses the gap in knowledge by combining the models from Ye et al. [8], Fabbro [16], Lankalapalli et al. [21] and Hann et al. [20] to predict the cross sectional melt pool geometry for a specified set of parameters and linking the predictions and corresponding experimental measurements to in-situ gathered pyrometric data. The model developed herein is detailed and its plausibility established through experimentation. Experiments were conducted on a powder-free tungsten substrate, where the aspect ratios were determined through metallographic cross sections and correlated with pyrometric signals analyzed via histographic methods. An interpretation of the results should provide insight into the importance of the pyrometric signals in determining cross sectional melt pool geometry. Additionally, the relationship between pyrometric signals and the geometry of the melt pool is investigated across different spot sizes to verify whether the model is consistent. As a secondary objective, this study also explores the impact of hatch distance on a powder free substrate.

2. Model

The model introduced in this paper builds upon the concept of dimensionless enthalpy initially proposed by Hann et al. [20]. Modifications have been made to the original framework, with a comprehensive derivation available in Appendix A. The foundation of the model lies in the factorless, dimensionless enthalpy ΔH_f, articulated by Eq. (1a):

$$\Delta H_f = \frac{P}{h_m \sqrt{\alpha v \left(\frac{\sigma}{2}\right)^3}}, \tag{1a}$$

$$\Delta H = G \cdot \Delta H_f \cdot \eta. \tag{1b}$$

In this context, P, v, and σ represent the laser power, speed, and spot size ($1/e^2$), respectively. The term $\alpha = k/(c_p \rho)$ defines the thermal diffusivity of the material, where k is the thermal conductivity, c_p the specific heat, and ρ the density of the material. The enthalpy required for melting, denoted as h_m, is given by $h_m = c_p \rho (T_m - T_0)$, with T_m representing the melting point and T_0 the initial temperature, following the remarks set by Fabbro [16]. It is important to note that the spot size σ is considered as the width of the keyhole [32, 33]. Additionally, the depth of the keyhole is assumed to be approximately equal to the melt pool depth.

The definition of the dimensionless enthalpy ΔH, as presented in Eq. (1b), commonly incorporates G, which represents a geometric factor determined by the assumed energy distribution of the laser (e.g. $G = 1/\pi$ [8]). Further, the absorptance factor η is usually included as shown in Eq. (1b). In this study, the geometry factor is chosen to be $G = (2/\pi)^{3/4}$. The reasoning for this can be found in Appendix A. Discussion on the absorptance η is provided later in the text.

A successful LPBF process, with minimal induced defects, typically occurs near the conduction-keyhole transition, with a stable keyhole [12, 16, 17]. Therefore, to design experiments that elucidate the LPBF process, it is essential to choose parameter sets (different combinations of primary laser parameters) that result in melt pool geometries within this region. To evaluate the proximity of a given parameter set to the transition region, the formalism presented by Lankalapalli et al. [21] was employed to estimate the melt pool depth d of a parameter set beforehand. Division by the spot size σ yields the aspect ratio $\mathrm{AR} = d/\sigma$. Further, the dimensionless enthalpy, as demonstrated by Fabbro [16] can be incorporated into the formalism of Lankalapalli et al. [21] to derive Eqs. (2a) and (2b):

$$\mathrm{AR} = \frac{d}{\sigma} = \Delta H_f \frac{\sqrt{Pe}}{2} \frac{T_m - T_0}{T_v - T_0} \frac{1}{g(Pe)}, \tag{2a}$$

$$\begin{aligned} g(Pe) = &\int_0^{2\pi} -Pe\, e^{-Pe\cos(\theta)} \\ &\cdot \left[\sum_{n=0}^{\infty} \epsilon_n I_n(Pe) \cos(n\theta) \left(\frac{n}{Pe} - \frac{K_{n+1}(Pe)}{K_n(Pe)} - \cos(\theta) \right) \right]. \end{aligned} \tag{2b}$$

Where $Pe = v\sigma/(2\alpha)$ represents the Péclet number and T_v denotes the boiling point. The function $g(Pe)$ characterizes the temperature gradient in dependence of Pe within a cylindrical keyhole, the walls of which are at temperature T_v. Within Eq. (2b), I_n and K_n refer to modified Bessel functions of the first and second kind, respectively, and of the n^{th} order. The term ϵ_n is defined as 1 for $n = 0$ and 2 for $\epsilon_n \geq 1$, as described by Lankalapalli et al. [21]. In the context of this study, keyholing is defined by an aspect ratio $d/\sigma \geq 1$. Conversely, the conduction mode is signified when the aspect ratio $d/\sigma \leq 1$. Based on this definition, Eq. (2a) can be rearranged to compute the theoretical required dimensionless enthalpy at the point where the transition from conduction mode to keyhole mode occurs, as shown in Eq. (3).

$$\Delta H_f|_{d/\sigma=1} = \frac{2}{\sqrt{Pe}} \frac{T_v - T_0}{T_m - T_0}\, g(Pe). \tag{3}$$

A notable challenge arises from the interdependence between absorptance and dimensionless enthalpy, creating a chicken-and-egg dilemma. A particular dimensionless enthalpy is associated with a specific geometry, as noted by Hann et al. [20], which subsequently influences the absorptance [9, 10, 32, 41]. Note, that a change in absorptance changes the enthalpy, which in turn changes the geometry. Nonetheless, to calculate ΔH in advance, knowledge of η is necessary. This challenge can be addressed by consulting the results of Ye et al. [8], which show that the trend of increasing absorptance with ΔH_f remains consistent across various materials. The study by Ye et al. [8] provides a description of the absorptance $\eta\left(\Delta H_f\right)$, as outlined in Eq. (4):

$$\eta = \eta_{\text{max}} \cdot (1 - e^{-0.66\,\eta_{\text{min}}\Delta H_f/(\pi\sqrt{Pe})}). \tag{4}$$

Where $\eta_{\text{max}} = 0.7$ denotes the plateau of absorbtion [8] and η_{min} denotes the minimal absorptance of the material used.

The culmination of the theoretical arguments presented can be seen in Eq. (5). As a measure to determine if a parameter set is close to the conduction-keyhole transition, the enthalpy threshold difference (ETD) is calculated according to Eq. (5). Parameter sets resulting in ETD < 0 are more likely to be in the conduction regime, whereas those with ETD ≥ 0 fall into the keyhole regime.

$$\begin{aligned}\text{ETD} &= \Delta H - \Delta H|_{d/\sigma=1} = \\ &G\eta_{\text{max}}\left(1 - e^{-0.66\eta_{\text{min}}\Delta H_f/(\pi\sqrt{Pe})}\right)\cdot\left(\Delta H_f - \Delta H_f|_{d/\sigma=1}\right).\end{aligned} \tag{5}$$

A fundamental premise of the model proposed by Lankalapalli et al. [21] is the insignificance of heat conduction into the part in the z-direction[2], which holds true if the thermal diffusion length $\delta = \sqrt{\alpha\sigma/(2v)} < \sigma/2$ [8]. Consequently, for this assumption to be valid, the condition $2\alpha/\sigma < v$ needs to be met[3]. This has to be taken into consideration when utilizing the presented model to choose parameter sets.

In this study, unlike in the approaches of Fabbro [16] and Lankalapalli et al. [21], Eq. (2b) was not approximated by polynomial or linear functions. It was determined numerically by summing 100 terms, ensuring rapid convergence of the sum function with higher-order terms contributing changes on the order of 10^{-6}. This numerical method is applicable for Péclet numbers up to 15, which typically surpasses the range observed in LPBF processes. For example, the parameter combination $\left\{v = 4\,\text{m}\,\text{s}^{-1}; \sigma = 80\,\mu\text{m}\right\}$ results in a Péclet number of approximately 9, whereas $\left\{v = 0.6\,\text{m}\,\text{s}^{-1}; \sigma = 80\,\mu\text{m}\right\}$ leads to a Péclet number of approximately 1. It should be noted that the first example represents an excessively high speed, which is not realistic for current LPBF processes. However, it could still be

[2]Consider that the laser scans on the plane given by the x- and y- direction

[3]Note that the thermal diffusion depth shown here is an approximation when used in the context of Gaussian beams. In order to verify whether the model can be used this approximation is sufficient. Nevertheless, a discussion on the thermal diffusion depth can be found in Appendix A

Table 1
Thermodynamic quantities of tungsten used (* near liquidus)

Symbol	Value	Unit	Reference
ρ *	17 200	$\mathrm{kg\,m^{-3}}$	[42]
c_p *	308	$\mathrm{J\,kg^{-1}\,K^{-1}}$	[43]
$\eta_{\min}$	0.26		[41]
k *	92	$\mathrm{W\,m^{-1}\,K}$	[44]
T_m	3695	K	
T_v	5828	K	
T_0	300	K	

incorporated into the model, provided the condition for thermal diffusion in the z-direction is met. Additionally, the method employed for computing $f(Pe)$ is computationally efficient, taking only minutes to process 100 parameter sets on a standard office PC.

3. Methodology

3.1. Experimental

Based on the model outlined in Section 2, calculations were performed for over 200 different parameter sets. The thermodynamic quantities used for the calculations can be found in Table 1. Out of these, 18 combinations were selected so that the ETD and predicted AR is situated, between −3.5 to 16 and between 0.5 to 2.2 respectively. The primary laser parameters varied within the following ranges: power between 400 W to 900 W, speed between $0.1\,\mathrm{m\,s^{-1}}$ to $1.7\,\mathrm{m\,s^{-1}}$, and spot sizes of 80 μm, 120 μm and 160 μm. The Péclet numbers selected for this study ranged from 0.4 to 6. It is important to note that Eq. (2b) was individually computed for each of the 200 parameter combinations, ensuring a unique comparison of each parameter against its corresponding threshold, according to Eq. (3).

Each selected parameter set was applied to three hatch blocks, as illustrated in Fig. 1, with varying hatch distances. These distances corresponded to overlaps of 75 %, 50 %, and 25 % relative to the utilized spot size. Hatch blocks have been assigned a width of 1 mm. The number of hatch lines used varied depending on the hatch distance to fill the width of a hatch block adequately. The length of each hatch block was consistently maintained at 30 mm, in order to reduce the thermal effect each line has on the next one. The hatch blocks were created on an Aconity 3D Midi (Aconity3D GmbH, Germany, Herzogenrath).

All hatch blocks were created on a powder-free tungsten substrate. As noted by Scipioni Bertoli et al. [25], powder in front of the laser beam typically melts by the time the laser reaches the location of the particle. This implies that the laser primarily interacts with the substrate and the molten material, similar to laser-welding processes as discussed by Ye et al. [8].[4] Additionally, Trapp et al. [41] found that the absorptance, linked to the melt pool geometry as

[4] Consequently, the thermodynamic quantities presented in Table 1 are set close to the melting point of tungsten

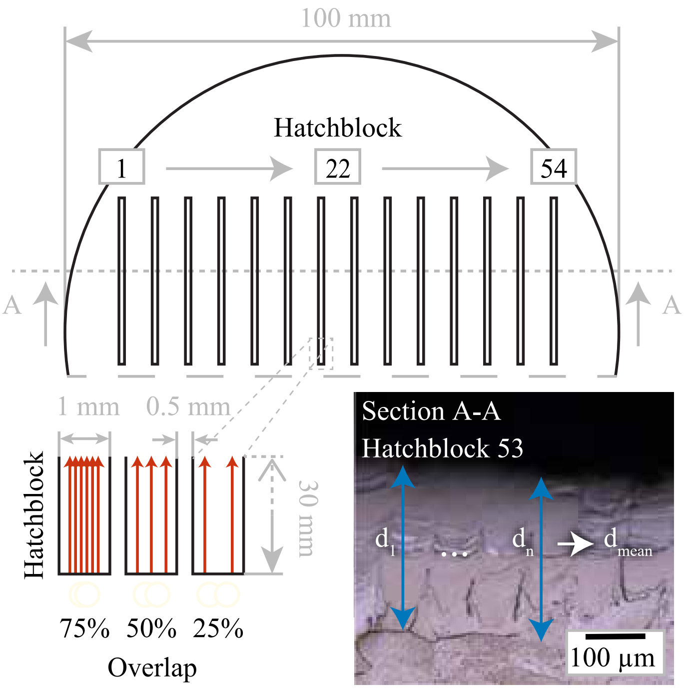

Figure 1: Illustration of the experimental setup: 18 parameter sets were selected based on the model described in Section 2. These parameter sets were utilized in conjunction with various hatch distances, corresponding to spot overlaps of 75 %, 50 %, and 35 %. Hatch blocks were sectioned using wire electrical discharge machining (WEDM), as indicated by the cut line A-A. The lower half was further reduced by approximately 4 mm in height, through grinding. Cross sections were metallographically prepared and imaged. The depth of each individual hatch line was measured, and the mean and standard deviation of these depths were calculated for each hatch block.

indicated by Simonds et al. [32], remains qualitatively unchanged with or without powder in the context of keyholing. Bitharas et al. [45] observed that the presence of a powder layer does not alter melt pool geometry. These observations provide a rationale for employing laser-welding models [20, 21] alongside a powder-free substrate to analyze the LPBF process. Due to the anticipated more dynamic environment resulting from the use of powder [17, 26], it was omitted to facilitate an understanding of the principal usability of the pyrometer in determining the melt pool geometry. The substrate surface used for the experiment was smoothed using a plane grinder, resulting in a surface roughness R_a of approximately 2 µm.

The powder-free substrate containing the hatch blocks was partitioned using wire electrical discharge machining (WEDM) on a Sodic VZ300L (Sodick Co., Ltd, Yokohama, Japan) as shown in Fig. 1. Subsequently, one half was ground down about 4 mm with a plane grinder in order to measure the depth of the melt pool at two different locations along the hatch block.

The metallographic preparation of the partitioned cross sections involved grinding using SiC paper with sequential grit sizes of 220, 500, 800 and 1000. Subsequent fine grinding was done on a Struers Largo using a 9 µm Diamond-Water Suspension (Dia-Pro). Post-Grinding, the polishing process comprised two stages: a 3 µm step using Struers

Floc and a 1 µm step with Struers Nap. To improve the visibility of grain boundaries and the melt pool, Murakami's etchant [46] was applied to the samples. Metallographic imaging was conducted using an Alicona InfiniteFocus G5+ (Alicona Imaging GmbH, Raaba, Austria). Images from both cross sections were measured using ImgageJ [47] as shown in Fig. 1. With the obtained depth the measured aspect ratio could be defined as the ratio between measured depth and spot size d/σ.

3.2. Pyrometric Data

Pyrometric data was collected for each hatch block using a Kleiber KG 740-LO pyrometer (Kleiber Infrared GmbH, Unterwellenborn, Germany). The employed pyrometer recorded the raw signal in mV at a polling rate of 100 kHz. The position of each measurement was determined using the data from the laser scanning system, as the two systems are interconnected. The wavelength of light to which this pyrometer is sensitive was 1753 nm. The measurement area was a circular region with a diameter of approximately 300 µm, concentric to the laser spot. The setup is depicted in Fig. 2.

The concentricity of the pyrometer measurement spot and the laser spot was verified through preliminary experiments. These experiments involved creating hatch patterns in six different scanning directions. The collected pyrometric data were analyzed to identify any directional bias towards higher or lower signals. The system's optical lenses were adjusted until no directional bias was observed, and the signal was maximized, ensuring adequate concentricity between the pyrometer measurement spot and the laser spot. Although a pyrometer was used in this study, temperature calibration was unnecessary, as only the raw signal was analyzed.

The analysis of the raw data was conducted using a script developed in-house. The dataset comprised approximately 11 million lines, making the full analysis and graphical representation computationally demanding. The primary function of the custom-developed script involves creating a 2D array, where each element corresponds to a 20 µm × 20 µm area. Every measured data point was allocated to one element of this array. In instances where multiple measurements corresponded to the same coordinates within the predefined array, the highest value was selected to represent the pixel in question. The choice of 20 µm as the element size was a compromise to balance resolution with data volume. The generated image size was 1622 px × 3819 px, which, even with the smallest spot size utilized in these experiments, suffices to distinctly resolve the melt pool. A schematic illustrating this algorithm can be found in Fig. 2. To mitigate signal noise, a background analysis was conducted. This involved tracking the laser scanning path with deactivated laser, a process repeated six times. This yielded data on signal noise encompassing approximately 66 million points. To ensure the integrity of the data presented in this work, the maximum intensity value from these 66 million points was identified (875 mV) and subsequently subtracted from all points in the actual data, before mapping to the array occurred.

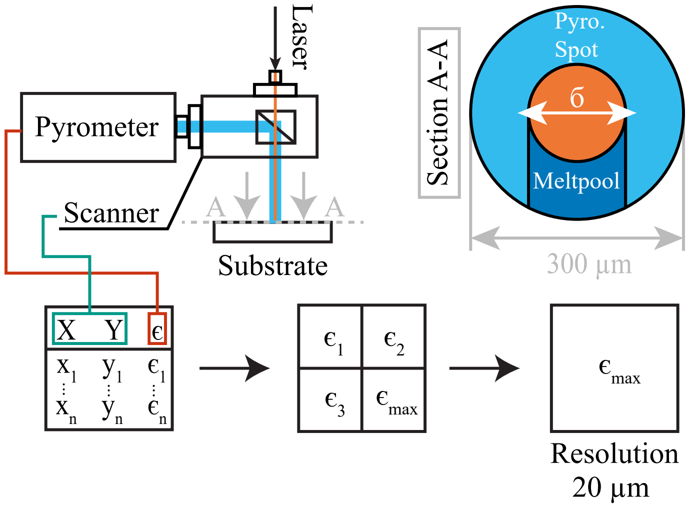

Figure 2: Pyrometric data was captured within an area given by a measurement spot diameter of 300 µm, concentric to the laser spot. The laser scanner system and the pyrometer were interconnected, allowing for synchronized data acquisition. Pyrometer measurements, recorded at a polling rate of 100 kHz, were associated with xy-positions obtained from the laser scanning system and presented in a tabular format. An in-house developed script aligned the tabulated data with an array, where each array element represented an area of 20 µm × 20 µm.

A section of the resultant image is displayed in Fig. 3. It should be noted that this image only illustrates five out of the 54 hatch blocks created. For a detailed analysis, the image was segmented into individual hatch blocks, facilitated by precise knowledge of the spacing and positions of the hatch blocks. For each hatch block histograms with a bin size of 15 mV were created. Note that the bin size was chosen as the ceiling of the standart deviation of the background signal. A representative excerpt of the 54 created histograms can be seen in Fig. 6. The created histograms show a set of distinct peaks. A Gaussian Mixture Model (GMM) [48] was employed to identify the position and shape of all modes in the histogram data. Each hatch block was used to train a separate GMM model utilizing the entire dataset. This resulted in 54 different models describing the 54 different histograms. The determination of the number of components of each histogram was informed by using the Bayesian Information Criterion (BIC) in the range 0 to 5 components. The selection process involved choosing the number of components based on the minimum BIC value with the highest gradient, alongside visual analysis by the author. The mean value and standard deviation of each Gaussian peak were extracted for each histogram.

4. Results and Discussion

4.1. Model Validation

No influence of the hatch distance on melt pool depth was observed, attributed to the chosen hatch line length ensuring uniform thermal conditions for each line. Hence, three hatch blocks, despite having different hatch distances but identical laser speed, spot, and power, are grouped into a single parameter set. Consequently, the 54 hatch blocks

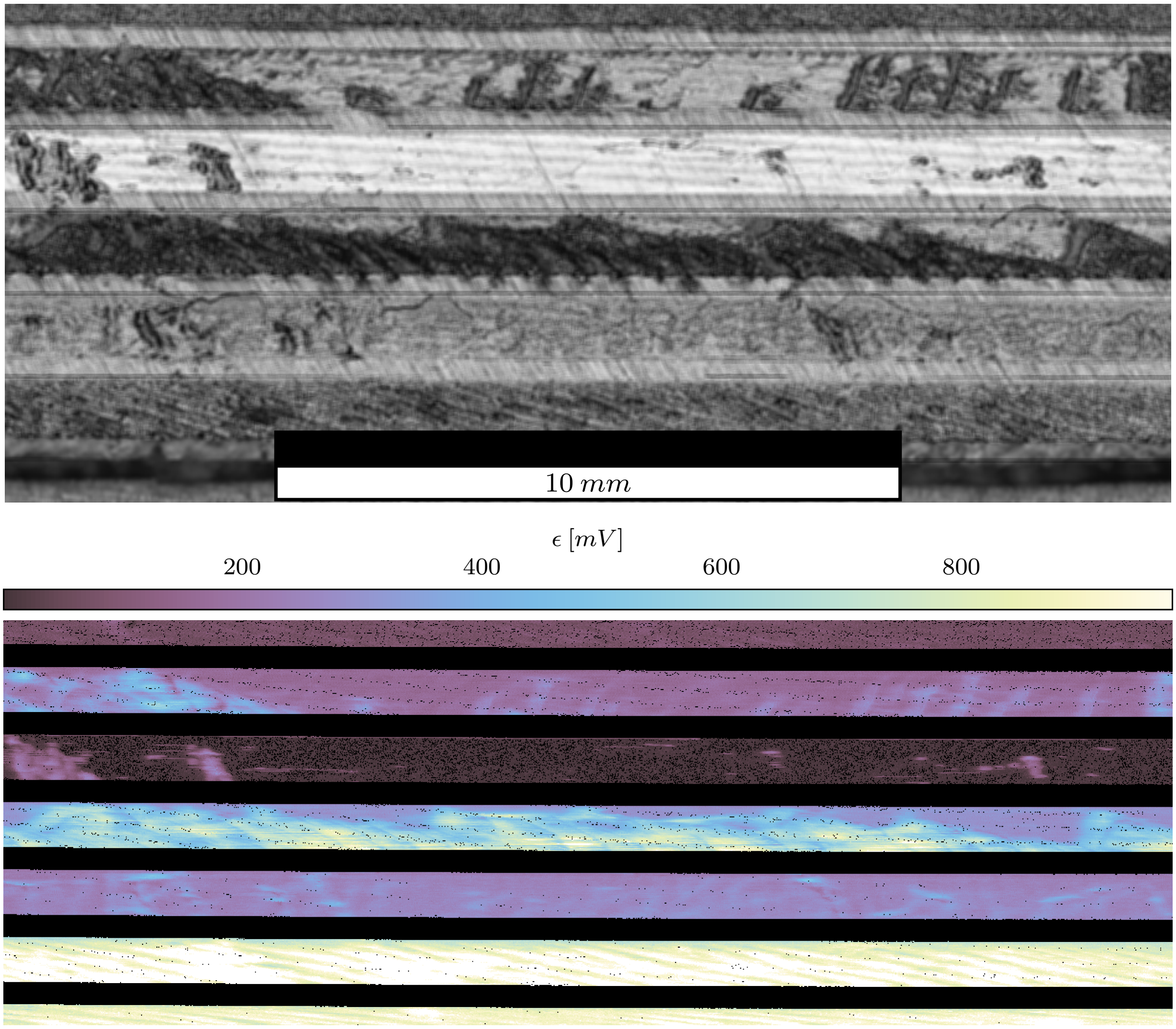

Figure 3: Optical image (top) and pyrometric image (bottom): Several defects (changes in surface quality) are visible in the optical image that correspond to signal changes in the pyrometric data. Each hatch block presented was created with different primary laser parameters. Note that changes in parameters can be identified by a change in the mean signal of each hatch block (qualitatively). Note that a small amount of aliasing could not be avoided.

created in this study can be condensed into 18 parameter sets. The measured depths (see Fig. 1 on how measurements were performed), representing an average from six unique positions on the substrate across multiple hatch lines, ensured statistically significant measurements. Fig. 4 illustrates the applicability of the model described in Section 2. Taking into account the measurement uncertainty, 16 out of 18 AR were correctly predicted. A linear relationship between dimensionless enthalpy and aspect ratio was established, corroborating findings by several researchers [8, 20, 49]. Remarkably, Fig. 4 shows that parameter sets with varying spot sizes but comparable ETD were also well predicted, and yield similar AR. The illustrated range in Fig. 4 of ETD between -3.5 to 16 corresponds to dimensionless enthalpies

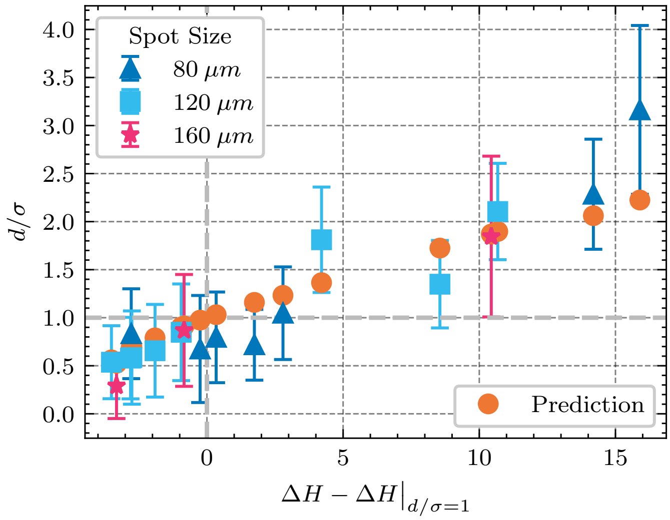

Figure 4: Agreement between model prediction and experimental results: Approximately 90 % of the predictions fell within the margins of error for experimentally measured values. A linear relationship between AR and ETD could be established. Parameters with different spot sizes but comparable ETD yield similar AR

between 14 to 39 in Hann et al. [20], 2 to 8 in King et al. [49] and Forien et al. [12] and 1 to 15 in Ye et al. [8][5]. As already noticed by Ye et al. [8] the utilization of a variable η yields a single linear response, eliminating the slope change observed by King et al. [49], Hann et al. [20] and Fabbro [16]. Note, that in the range presented here, the slope change should be evident.

4.2. Pyrometric Data

4.2.1. Pyrometric Image

Fig. 3 displays a comparison between the pyrometric data acquired and an optical image of the hatch blocks. The creation of these hatch blocks introduced defects such as sudden changes in surface quality, as evidenced by their comparison. The defects correspond to areas with elevated pyrometric signals, a relationship that aligns with findings from prior research on the potential of using pyrometric signals to identify common defects in LPBF processes [50]. However, the details regarding this correlation remain a subject of discussion [38]. Note that as some defects correlate with the melt pool geometry, as described in Section 1, a correlation between some types of defects and pyrometric signals is plausible. Following the acquisition of pyrometric data, each of the 54 hatch blocks was segmented, and a histogram for each segmented hatch block was produced, employing the methodology described in Section 3. Representative histograms can be found in Fig. 6

[5]For the comparison to Hann et al. [20] and King et al. [49] a fixed $\eta = 0.4$ was used. For the comparison to Ye et al. [8] a variable η according to Eq. (4) was used

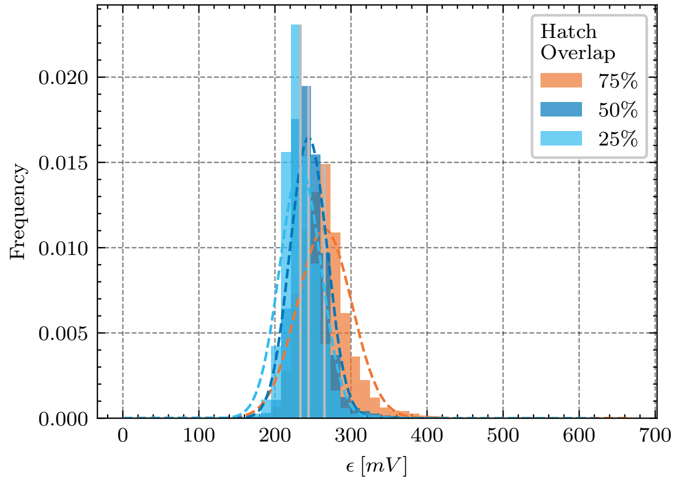

Figure 5: Influence of hatch distance on pyrometric signal: Considering the histograms of hatch blocks created under identical primary laser parameters yet with varying hatch distances, a negligible difference in the position of the main mode is observed, considering the intrinsic variability (15 mV) of the signal and the change that occurs due to a change in primary laser parameters.

4.2.2. Histographic Data

Figure 5 displays the typical variation in pyrometric signal for a single parameter set (comprising laser power, speed, and spot size) produced using different hatch distances. Note that this sample is representative of the entire dataset. Thus, for the purposes of this study, the assumption that hatch distance does not significantly impact the pyrometric signal is justified. Note that changes in primary laser parameters yield much greater changes than the changes presented in Fig. 5. This allows for the consideration of different hatch distances as a unified parameter set in further analysis. Note that this is mainly due to the length of the hatch blocks used in this study. As illustrated by Renken et al. [39], the pyrometric signal can change depending on local environmental circumstances.

Reviewing Fig. 6, the histograms of hatch blocks with different ETD are presented. A significant portion, 74 % of the histograms, exhibit a monomodal distribution, whereas 26 % display a multimodal distribution of signals. Multimodal distributions predominantly occur in parameter sets where ETD ≤ 0. Additionally, parameter sets where ETD $\gg 0$ are likely to show broader distributions, with their mean mode shifted towards higher signal values. These observations regarding histogram morphology align with the findings of Forien et al. [12].[6]

4.2.3. Principal Mode Data Collapse

The mean signal of the principal mode from histograms was selected to represent the pyrometric signal, with the standard deviation of the Gaussian fit being used as measurement uncertainty. Presenting the data in this manner and

[6] Given that Forien et al. [12] conducted their research using a different material and a fixed absorptance, discrepancies in their findings compared to the current study are anticipated. However, the extent of peak broadening observed in the high-enthalpy regime of this study was not reported by Forien et al. [12], despite the comparable enthalpy ranges. The origin of this discrepancy remains uncertain, underscoring the need for additional research to elucidate these differences.

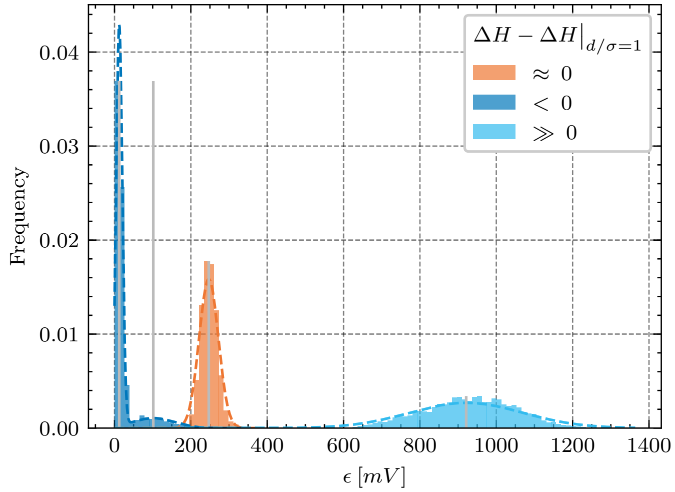

Figure 6: Histograms of hatch blocks with different ETD: Analysis shows that most histogram distributions can be approximated by a single Gaussian peak. Parameters with ETD ≤ 0 show a multimodal distribution. The higher ETD, the higher the spread of the signal.

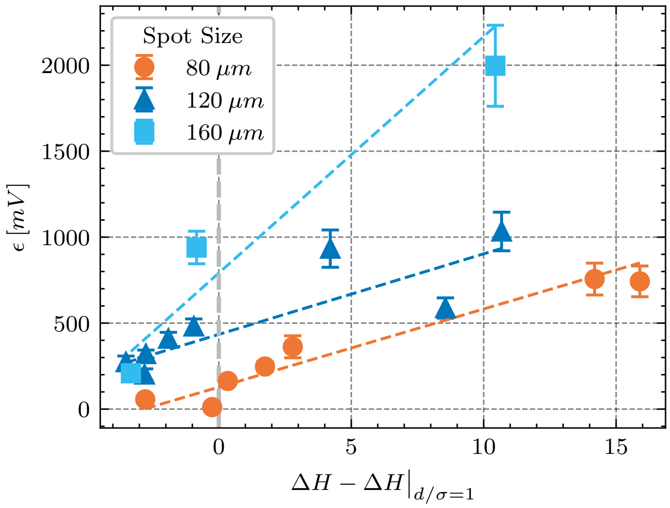

Figure 7: Pyrometric signal vs. ETD for different laser spot sizes. A separate linear relationship for each spot size can be found between signal intensity and ETD, which is plausible considering the results of Forien et al. [12]

plotting it against ETD, as shown in Fig. 7, reveals that distinct linear relationships between the pyrometric signal ϵ exist for each of the investigated spot sizes. Note that a linear trend was also observed by Forien et al. [12] for one specific spotsize.The consistency of the pyrometer signal across different spot sizes suggests it may contain information about the melt pool geometry, raising the question of whether this relationship can be substantiated on a physical basis.

The pyrometer measures the intensity of radiation at a specific wavelength. As depicted in Fig. 7, an increase in ETD correlates with a rise in signal intensity. Concurrently, the model verified indicates that an increase in ETD results in a higher AR. The width of the keyhole, approximately constant and determined by the chosen spot size [32], suggests

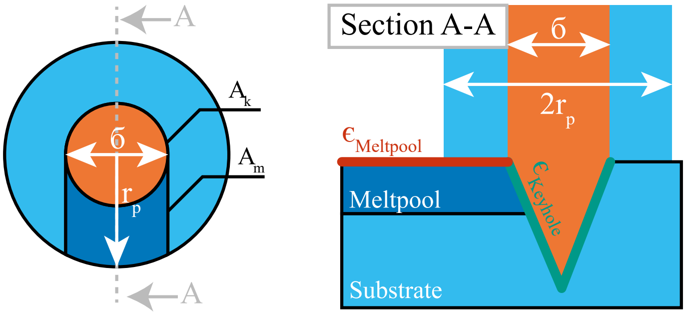

Figure 8: Approximation of the geometries involved: The keyhole can be approximated by a cone with diameter σ. The measurment spot of the pyrometer is given by the radius r_p. For small aspect ratios the emissive surfaces of the melt pool A_m and the keyhole A_k are in a comparable range. Considering the temperature difference it is argued that the main contribution to the pyrometer signal is given by the emissive suface of the keyhole A_k.

that an increase in AR primarily stems from a deeper keyhole. Considering the impact on the light-emitting surface detected by the pyrometer, a deeper keyhole enlarges its surface area, thereby creating more radiative surface, which leads to an enhanced signal.

To understand the effect of a changing radiative surface, approximating the geometries of the melt pool and keyhole, as illustrated in Fig. 8, proves useful. The keyhole is roughly conical, with its base diameter determined by the laser spot size [21, 32]. The depth for a given parameter set can be estimated using the model outlined in Section 2 and verified in Fig. 4. Thus, the radiative surface of the keyhole can be expressed as $A_k = \pi\sigma/2 \cdot \sqrt{d^2 + (\sigma/2)^2}$. Additionally, the radiative surface of the melt pool can be approximated by $A_m = \sigma r_p - \pi\,(\sigma/2)^2$, where r_p represents the radius of the pyrometer measurement spot, as depicted in Fig. 8.

In order to compare the radiative contributions of melt pool and keyhole, the temperatures involved need to be approximated. The walls of the keyhole are maintained at the vaporization temperature of tungsten, which is $T_v = 5828\,\text{K}$. The thermal gradient (TG) is approximately $30\,\text{K}\,\mu\text{m}^{-1}$ [51, 52]. Given the diameter of the pyrometer spot, the temperature at the edge of the pyrometer measurement spot can be determined by calculating $T_e = T_v - \text{TG}\cdot(r_p - \sigma/2)$. For the sake of argument the temperature of the radiative surface from the melt pool A_m is set equal to $T_m = (T_e + T_v)/2$, which represents the average temperature between the edge and the vaporization temperature.

Based on Planck's radiation law for ideal black bodies, the band radiance for the wavelength utilized by the pyrometer used in this study can be determined by performing an integration over λ within the limits $\lambda_1 = 1748\,\text{nm}$ and $\lambda_2 = 1758\,\text{nm}$[7], as shown in Eq. (6a).

$$B(T) = \int_{\lambda_1}^{\lambda_2} \frac{2hc^2}{\lambda^5} \frac{1}{e^{\frac{hc}{\lambda k_B T}} - 1}\, d\lambda. \tag{6a}$$

[7] It should be noted that the specific wavelength band to which the pyrometer responds was not specified. For the purposes of this analysis, an assumption was made to consider a wavelength band of 10 nm, symmetrically centered around the nominal sensitivity wavelength of 1753 nm. It is crucial to emphasize that variations in the width of the assumed wavelength band do not significantly impact the conclusions derived from this analysis.

Here, λ represents the wavelength of the observed radiation, h is the Planck constant, c denotes the speed of light, k_B is the boltzmann constant, and T refers to the temperature at which the distribution is calculated.

By multiplying the previously calculated emitting surface areas of the melt pool and the keyhole with their respective band radiances, denoted as $B(T_v) \cdot A_k$ and $B(T_e) \cdot A_m$ respectively, it becomes possible to compare the estimated contributions to the pyrometric signal. For spot sizes within the range of 80 µm, 120 µm and 160 µm, AR from 0.7 to 2, and a pyrometer measurement spot size of 300 µm, it is estimated that the contribution of the keyhole to the total emitted power ranges from 82 % to 93 %.

The observation that the keyhole contributes significantly to the total emitted power is not surprising, especially when considering that even small keyholes created by a spot size of 80 µm and an aspect ratio of 0.7 possess approximately the same surface area as the melt pool, without accounting for the differences in radiation intensity due to the temperature of the emitting surface.[8] It is important to note that the area of the radiative surface of the melt pool A_m primarily scales with the spot size, whereas the radiative surface of the keyhole A_k also scales with the depth. According to Simonds et al. [32], depth oscillations by a factor of 2 occur at a frequency of 10 kHz, significantly affecting A_k and consequently leading to an even higher contribution of A_k compared to A_m in the total received pyrometric signal. Furthermore, this analysis does not consider the idea proposed by Lane et al. [36], which suggests that the keyhole, due to its geometric nature, emits radiation in a more directed manner, as opposed to the more diffuse emission from shallow melt pools. If applicable, it would further exaggerate the contribution of the keyhole to the total signal measured by such a setup, still without taking into acount the difference in band radiance due to the temperature (see Fig. 10). These arguments lead to the conclusion that the keyhole area is the primary contributor to the total measured pyrometric intensity.

In Fig. 7, it is demonstrated that the received pyrometric signal exhibits linear relationships for different spot sizes. It was already argued that the primary component of the pyrometric signal is the keyhole surface area A_k. To elucidate the scaling behaviour observed in Fig. 7 for different spot sizes, consider what would happen to the pyrometric signal, for parameter sets that have the same AR but different spot sizes.

The surface area of the keyhole, which is proportional to the recieved pyrometric signal, can be expressed in terms of the aspect ratio $\epsilon \propto A_k = \pi(\sigma/2)^2 \cdot \sqrt{4(d/\sigma)^2 + 1}$. When considering two different signals originating from keyholes with identical aspect ratios but different spot sizes, characterized by $\epsilon_1, d_1, \sigma_1$ and $\epsilon_2, d_2, \sigma_2$, where $d_1/\sigma_1 = d_2/\sigma_2$, it follows that $\epsilon_1/\sigma_1^2 = \epsilon_2/\sigma_2^2$. This implies that the received pyrometric signal scales with σ^2. By applying a normalization of σ^2 to the data presented in Fig. 7, Fig. 9 is obtained. It is observed that the linear scaling previously noted for different spot sizes in Fig. 7 converges onto a single line, defining the scaling relationship between ETD and the received, normalized pyrometric signal ϵ/σ^2.

[8] Even when a pyrometer with a larger measurement spot is utilized, accounting for the temperature difference renders the contribution of the melt pool as negligible compared to the keyhole.

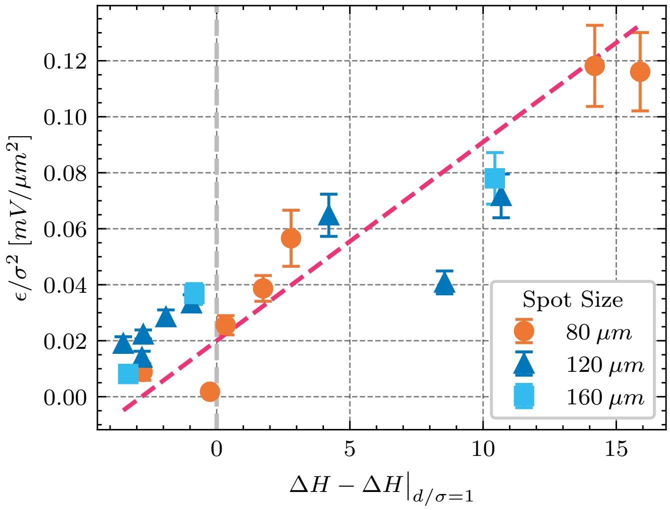

Figure 9: Normalized pyrometric signal vs. ETD. By normalizing pyrometric data to the spot size used, a single linear scaling between ETD and the recieved pyrometer signal can be obtained, implying a relationship between keyhole geometry and pyrometeric signal.

To conclude this line of reasoning, recall the model described in Section 2 and verified by Fig. 4, where it was demonstrated that ETD scales linearly with the aspect ratio AR of the keyhole. It has been shown that parameter sets with different spot sizes and similar ETD yield comparable AR. Additionally, in Fig. 9, a linear scaling between ETD and the normalized pyrometric signal ϵ/σ^2 was established. Therefore, by the argument of transitivity, a linear scaling between the normalized pyrometric signal ϵ/σ^2 and AR must exist. As demonstrated by Simonds et al. [32], changes in the keyhole width for a given spot size are negligible compared to changes in depth, positioning the depth of the keyhole as the principal variable determining the intensity of the pyrometric signal in this scenario.[9]

The results discussed are specific to tungsten, prompting curiosity about the possibility of similar scaling between keyhole geometry and pyrometric signal for different materials. By applying the same approximations with adjustments for the temperatures involved, insights into different materials can be obtained. The keyhole walls are always at approximately their respective temperature of vaporization, T_v. In Fig. 10, the effect of a change in keyhole depth on the radiation intensity change is illustrated as a function of temperature. For instance, for tungsten, the difference in the received signal for a keyhole depth change from 40 µm to 160 µm is approximately 0.32 mW sr^{-1}. For aluminum, this difference shifts to 0.06 mW sr^{-1}. Therefore, the ability to resolve differences in depth may depend on the material and the pyrometer used. The higher the vaporization temperature, T_v, of the metal observed via pyrometry, the better the resolvability of different depths.

[9] As can be inferred from references [8, 9, 25, 32, 33, 36], the presence of powder should only lead to more noise in the signal without changing the fundemental relationship between the depth and pyrometric signal.

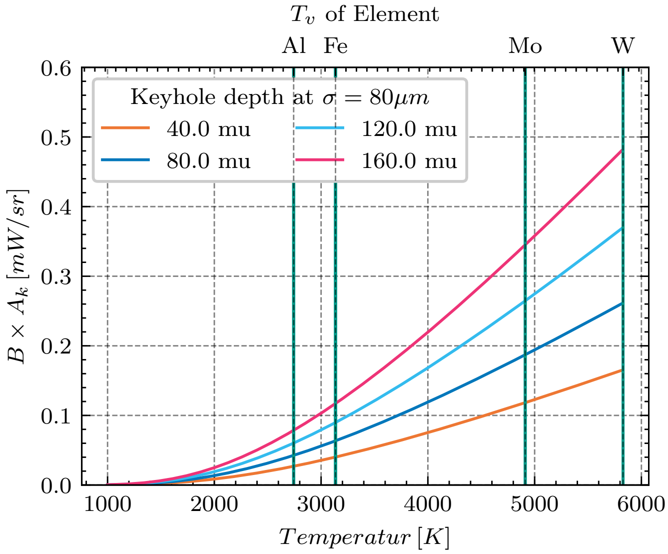

Figure 10: Emission strength of a keyhole at different depths as function of temperature: For materials with a high temperature of vaporization T_v, oscillations in depth yield a higher difference in emission than for materails with a lower temperature of vaporization. Resolvability of depth changes by pyrometric signals is therefore dependent on the material observed.

4.2.4. Interpretation of Histograms

It has been demonstrated that the pyrometric signal provides insights into the size of the emitting surface, thereby shedding light on the aspect ratio of the keyhole. This suggests that the morphologies of the histograms depicted in Fig. 6 reflect changes in keyhole geometry. The multimodal nature of histograms associated with low-energy parameter sets (ETD < 1) supports the hypothesis that these multiple modes correspond to the unstable region identified by Fabbro [53], where changes between distinct geometries can occur. As the parameter ETD increases, a transition occurs towards a stable keyhole configuration characterized by a singular keyhole geometry and a Gaussian distribution in the pyrometric signal, indicating stability. Successful LPBF typically occurs within the keyhole regime prior to the emergence of keyhole instabilities [12], aligning with an AR between 1 to 1.7 or corrosponding to an ETD between 0 to 10. This is consistent with the observations by King et al. [49] and Forien et al. [12], though it is noted that Forien et al. [12] identifies an optimal parameter range slightly higher than what is suggested here, yet still within a comparable range. In the case of parameter sets with ETD $>> 1$, indicating high energy, the broad distribution of pyrometric signals imply a highly unstable keyhole, prone to frequent depth variations. Such instability and oscillations in depth are indicative of potential keyhole porosity, as described by Khairallah et al. [34], due to the formation of keyhole pores. It is important to note that the specific peak position of the signal depends on the pyrometer and the material used. In this case, the optimal position was identified to be approximately 400 mV above the noise floor.

5. Conclusion

In this publication a modified, dimensionless enthalpy model based on the findings of Ye et al. [8], Fabbro [16], Lankalapalli et al. [21] and Hann et al. [20] was presented. Predictions of the aspect ratio of a melt pool fit reasonably well to the experimental findings. The pyrometric signal of 54 hatch block experiments was analyzed consisting of 18 parameter sets (laser speed, spot size and power) and overlaps ranging from 35 % to 75 %. Histographic analysis of the received pyrometric data was carried out for each parameter set and compared to aspect ratios obtained via the measurment of metallographic cross sections and model predictions. Following conclusions can be drawn from the results presented here:

- The dimensionless enthalpy model presented herein enables the prediction of keyhole aspect ratios for various parameter sets. Moreover, it allows estimations when the spot sizes are altered. Parameters with comparable dimensionless enthalpy yield comparable aspect ratios. Further, because the melt pool depth can be approximated by the depth of a keyhole, concrete depths can be predicted by the model presented herein.
- The pyrometric signal primarily originates from the emitting surface of the keyhole, thereby enabeling the inference of the aspect ratio of the keyhole and, subsequently, its depth. The depth of the keyhole is approximately the depth of the melt pool, at least in the case of tungsten for typical LPBF conditions. The aspect ratio of the keyhole is linearly proportional to the pyrometric signal, normalized by the square of the corresponding laser spot size used. Note that the temperature of the keyhole wall is equal to the temperature of vaporization by necessity. Therfore, changes in the pyrometric signal are due to changes in the emitting surface.
- Histograms of pyrometric signals exhibit three distinct forms: multimodal, single modal narrow, and single modal wide, corresponding to low, medium, and high enthalpy inputs, respectively. It is posited that the shapes of these histograms reflect changes in aspect ratio, thereby encoding information about the stability of the LPBF process. Parameters conducive to stable LPBF conditions were identified as those leading to a relatively narrow, single modal distribution of the pyrometric signal. Because of the found relationship between the model and the pyrometric signal, it can be concluded that parameters suitable for LPBF of tungsten have an AR between 1 to 1.7 or ETD between 0 to 10 according to the model presented here. Comparison to prior studies done by other authors indicates that this range is the optimum for a multitude of materials.

This study provides a detailed physical description and interpretation of pyrometric signals and their correlation with the geometry of the keyhole observed in LPBF. It has been demonstrated by Renken et al. [39] that a closed feedback loop based on pyrometric data is feasible. Therefore, achieving in-situ control of melt pool geometry appears within grasp to the scientific community. However, investigations into materials other than tungsten are essential to determine whether the scaling described herein is universally applicable. Further, in-situ control could be used more generally in laser welding, as indicated by the results of Xiao et al. [54]. Note that the calculations presented here can be used to predict the depth of the meltpool. Additionally, translating this fundamental research into actual part manufacturing in LPBF should be pursued to investigate the relationship between melt pool stability and part quality.

CRediT authorship contribution statement

Janko Stajkovic: Conceptualization, Methodology, Software, Visualization, Formal analysis, Writing - Original Draft. **Manuel Kahl:** Investigation, Software, Data Curation, Validation, Writing - Review & Editing. **Lukas Kaserer:** Supervision,Validation, Writing - Review & Editing. **Jakob Braun:** Validation, Writing - Review & Editing. **Sophie Scheuringer:** Investigation. **Bernhard Mayr-Schmölzer:** Resources,Writing - Review & Editing. **Benedikt Distl:** Resources,Writing - Review & Editing. **Gerhard Leichtfried:** Supervision, Validation, Project administration, Funding acquisition, Writing - Review & Editing.

Declaration of Competing Interest

The authors declare that they have no known competing financial interests or personal relationships that could have appeared to influence the work reported in this paper.

Declaration of Generative AI and AI-assisted Technologies in the Writing Process

During the preparation of this work the author(s) used ChatGPT 4.0 in order to improve readability and correct spelling and grammatical errors. After using this tool/service, the author(s) reviewed and edited the content as needed and take(s) full responsibility for the content of the publication.

Data Availability

Data will be made available on request.

Acknowledgements

The authors would like to thank the Austrian Research Promotion Agency (FFG) for supporting the research [DB-NR: FO999902718].

Appendix

A. Derivation of the Dimensionless Enthalpy and Physical Description

The interpretation of the dimensionless enthalpy by King et al. [49] is revisited, where the fundamental concept is elucidated through the dwell time τ. The absorption of laser energy $\eta P\tau$ on the irradiated surface $\pi(\sigma/2)^2$, combined with thermal diffusion depth $\delta = \sqrt{\alpha\tau}$, constitute the non-normalized enthalpy. By dividing the absorbed energy by the volume determined by the surface area and thermal diffusion depth, an expression is derived that closely mirrors the formula for dimensionless enthalpy as defined by Hann et al. [20], differing only by the inclusion of a π instead of a $\sqrt{\pi}$ in the denominator. This discrepancy does not alter the physical interpretation but needs some clarification.

Consider the fundamental beam mode solution of the paraxial wave equation in cylindrical coordinates [55]. Let the coordinate system be defined such that the z axis aligns with the propagation direction of the Gaussian beam, which exhibits radial symmetry about this axis. Note that $z = 0$ is at the exact focus point of the Gaussian beam. The transverse electric field of any Super-Gaussian beam is described by Eq. (7):

$$E_z(r, n) = E(r, z = 0, n) = E_0 e^{\left(-\frac{r}{\omega_0}\right)^n}. \tag{7}$$

The transverse electric field of a Gaussian beam is obtained by $n = 2$, a Super-Gaussian beam is described by satisfying $2 < n < \infty$ and ideal flat top beam is obtained by $\lim_{n\to\infty} E_z(r, n)$. Note that therefore n describes the order of the Super-Gaussian beam and must satisfy $n \geq 2$, E_0 denotes the peak strength of the transverse electric field, at $r = 0$ and $z = 0$, ω_0 denotes the focus radius and r denotes the radial distance from the z axis. The intensity is given by $|E(r, z = 0, n)|^2/(2\beta)$ where the wave impedance is denoted by β. The total power of any order of a Super-Gaussian beam can be calculated by integrating the intensity with respect to the spatial coordinates as shown in Eq. (8)[10]:

$$\begin{aligned} P(n) &= 2\pi I_0 \int_0^\infty r e^{-2\left(\frac{r}{\omega_0}\right)^n} dr \\ &= 2^{-\frac{2}{n}} \Gamma\left(1 + \frac{2}{n}\right) I_0 \pi \omega_0^2. \end{aligned} \tag{8}$$

Γ denotes the gamma function, and $I_0 = E_0^2/(2\beta)$ represents the peak intensity at the origin of the coordinate system. Note that the power depends solely on the free variable n. By solving Eq. (8) for I_0, the peak intensity at the focus point is determined, as articulated by Eq. (9a):

[10] Note that the integral with respect to the azimuthal angle in the limits from 0 to 2π is already solved and given by the factor 2π. Therefore, this integral is omitted in the representation

$$I_0(n) = \frac{2^{\frac{2}{n}}}{\Gamma\left(1 + \frac{2}{n}\right)} \frac{P}{\pi w_0^2}, \tag{9a}$$

$$I_{0f} = \lim_{n \to \infty} I_0(n) = \frac{P}{\pi w_0^2}, \tag{9b}$$

$$I_{0g} = I_0(2) = \frac{2P}{\pi \omega_0^2}. \tag{9c}$$

For a Gaussian beam, where $n = 2$, the intensity is given by I_{0g}, as described in Eq. (9b), whereas a flat-top laser is described by I_{0f} in Eq. (9c). To describe the enthalpy in LPBF, it is necessary to multiply the peak intensity by the dwell time and the reciprocal of the thermal diffusion depth: $I_0 \tau \delta$.

For a transient Gaussian beam, it is necessary to consider that a Gaussian distribution is also present in temporal coordinates. The approach of Hann et al. [20] considers a Gaussian distribution of τ, as formulated in Eq. (10a):

$$\begin{aligned} \tau(n) &= 2 \int_0^\infty e^{-2\left(\frac{vt}{\omega_0}\right)^n} dt, \\ &= 2^{1-\frac{1}{n}} \Gamma\left(1 + \frac{1}{n}\right) \frac{\omega_0}{v}, \end{aligned} \tag{10a}$$

$$\tau_f = \lim_{n \to \infty} \tau(n) = \frac{2\omega_0}{v}, \tag{10b}$$

$$\tau_g = \tau(2) = \frac{\sqrt{\pi}\omega_0}{\sqrt{2}v}. \tag{10c}$$

Notice that for flat-top laser profiles, as described by τ_f in Eq. (10b), the conventionally used dwell time is obtained, whereas for a Gaussian temporal component, τ_g is given by Eq. (10c). Since the thermal diffusion depth δ depends on the choice of τ, a generalized expression for δ is obtained, as described in Eq. (11a):

$$\delta(n) = \sqrt{\alpha\tau} = 2^{\frac{1}{2} - \frac{1}{2n}} \sqrt{\Gamma\left(1 + \frac{1}{n}\right)} \sqrt{\frac{\alpha\omega_0}{v}}, \tag{11a}$$

$$\delta_f = \lim_{n \to \infty} \delta(n) = \sqrt{\frac{2\alpha\omega_0}{v}}, \tag{11b}$$

$$\delta_g = \delta(2) = \sqrt[4]{\frac{\pi}{2}} \sqrt{\frac{2\alpha\omega_0}{v}}. \tag{11c}$$

Analogously to the deliberation made for τ, the thermal diffusion depth for a flat-top laser profile is given by δ_f in Eq. (11b), whereas the thermal diffusion depth for a Gaussian beam is given by δ_g in Eq. (11c).

By combining Equations (9a) to (11c) in different ways, normalizing by the melting enthalpy h_m and multiplying by the absorptance η, the most common definitions of the dimensionless enthalpy ΔH can be obtained. By calculating $I_{0g}\tau_g/\delta_f$, the enthalpy definition of Hann et al. [20] is obtained, which yields a geometric factor $G = 1/\sqrt{\pi}$. The enthalpy described by King et al. [49] and Ye et al. [8] is obtained by calculating $I_{0f}\tau_f/\delta_f$, leading to the geometric factor $G = 1/\pi$. This derivation indicates that the geometric factor $G = 1/\pi$ is applied when describing a flat-top laser.

In this work, $G = (2/\pi)^{3/4}$ is utilized, derived by calculating $I_{0g}\tau_g/\delta_g$. However, the employment of one specific geometric factor does not alter the physical interpretation and significance of all correlations made to the dimensionless enthalpy.

References

[1] I. Yadroitsev, I. Yadroitsava, A. Plessis, E. MacDonald (Eds.), Fundamentals of laser powder bed fusion of metals, Additive manufacturing materials and technologies, Elsevier, Amsterdam, 2021.

[2] S. Chowdhury, N. Yadaiah, C. Prakash, S. Ramakrishna, S. Dixit, L. R. Gupta, D. Buddhi. Laser powder bed fusion: a state-of-the-art review of the technology, materials, properties & defects, and numerical modelling. JMR & T 20 (2022) 2109–2172. doi:10.1016/j.jmrt.2022.07.121.

[3] M. Grasso, A. Remani, A. Dickins, B. M. Colosimo, R. K. Leach. In-situ measurement and monitoring methods for metal powder bed fusion: an updated review. Meas. Sci. Technol. 32 (2021) 112001. doi:10.1088/1361-6501/ac0b6b.

[4] J. Xue, Z. Feng, J. Tang, C. Tang, Z. Zhao. Selective laser melting additive manufacturing of tungsten with niobium alloying: Microstructure and suppression mechanism of microcracks. J. Alloy. Compd. 874 (2021) 159879. doi:10.1016/j.jallcom.2021.159879.

[5] J. Huang, M. Li, J. Wang, Z. Pei, P. Mclntyre, C. Ma. Selective laser melting of tungsten: Effects of hatch distance and point distance on pore formation. J. Manuf. Processes 61 (2021) 296–302. doi:10.1016/j.jmapro.2020.11.034.

[6] Y. A. Mayi, M. Dal, P. Peyre, M. Bellet, C. Metton, C. Moriconi, R. Fabbro. Transient dynamics and stability of keyhole at threshold in laser powder bed fusion regime investigated by finite element modeling. J. Laser Appl. 33 (2021) 012024. doi:10.2351/7.0000330.

[7] V. Semak, A. Matsunawa. The role of recoil pressure in energy balance during laser materials processing. J. Phys. D 30 (1997) 2541–2552. doi:10.1088/0022-3727/30/18/008.

[8] J. Ye, S. A. Khairallah, A. M. Rubenchik, M. F. Crumb, G. Guss, J. Belak, M. J. Matthews. Energy coupling mechanisms and scaling behavior associated with laser powder bed fusion additive manufacturing. Adv. Eng. Mater. 21 (2019) 1900185. doi:10.1002/adem.201900185.

[9] T. R. Allen, W. Huang, J. R. Tanner, W. Tan, J. M. Fraser, B. J. Simonds. Energy-coupling mechanisms revealed through simultaneous keyhole depth and absorptance measurements during laser-metal processing. Phys. Rev. Appl. 13 (2020). doi:10.1103/physrevapplied.13.064070.

[10] M. Bayat, A. Thanki, S. Mohanty, A. Witvrouw, S. Yang, J. Thorborg, N. S. Tiedje, J. H. Hattel. Keyhole-induced porosities in laser-based powder bed fusion (l-pbf) of ti6al4v: High-fidelity modelling and experimental validation. Addit. Manuf. 30 (2019) 100835. doi:10.1016/j.addma.2019.100835.

[11] A. A. Martin, N. P. Calta, S. A. Khairallah, J. Wang, P. J. Depond, A. Y. Fong, V. Thampy, G. M. Guss, A. M. Kiss, K. H. Stone, C. J. Tassone, J. Nelson Weker, M. F. Toney, T. van Buuren, M. J. Matthews. Dynamics of pore formation during laser powder bed fusion additive manufacturing. Nat. Commun. 10 (2019) 1987. doi:10.1038/s41467-019-10009-2.

[12] J.-B. Forien, N. P. Calta, P. J. Depond, G. M. Guss, T. T. Roehling, M. J. Matthews. Detecting keyhole pore defects and monitoring process signatures during laser powder bed fusion: A correlation between in situ pyrometry and ex situ x-ray radiography. Addit. Manuf. 35 (2020) 101336. doi:10.1016/j.addma.2020.101336.

[13] M. Hamidi Nasab, G. Masinelli, C. de Formanoir, L. Schlenger, S. Van Petegem, R. Esmaeilzadeh, K. Wasmer, A. Ganvir, A. Salminen, F. Aymanns, F. Marone, V. Pandiyan, S. Goel, R. E. Logé. Harmonizing sound and light: X-ray imaging unveils acoustic signatures of stochastic inter-regime instabilities during laser melting. Nat. Commun. 14 (2023). doi:10.1038/s41467-023-43371-3.

[14] A. M. Kiss, A. Y. Fong, N. P. Calta, V. Thampy, A. A. Martin, P. J. Depond, J. Wang, M. J. Matthews, R. T. Ott, C. J. Tassone, K. H. Stone, M. J. Kramer, A. van Buuren, M. F. Toney, J. Nelson Weker. Laser–induced keyhole defect dynamics during metal additive manufacturing. Adv. Eng. Mater. 21 (2019) 1900455. doi:10.1002/adem.201900455.

[15] D.-Z. Wang, K.-L. Li, C.-F. Yu, J. Ma, W. Liu, Z.-J. Shen. Cracking behavior in additively manufactured pure tungsten. Acta Metall. Sinica 32 (2019) 127–135. doi:10.1007/s40195-018-0752-2.

[16] R. Fabbro. Scaling laws for the laser welding process in keyhole mode. J. Mater. Process. Tech. 264 (2019) 346–351. doi:10.1016/j.jmatprotec.2018.09.027.

[17] R. Cunningham, C. Zhao, N. Parab, C. Kantzos, J. Pauza, K. Fezzaa, T. Sun, A. D. Rollett. Keyhole threshold and morphology in laser melting revealed by ultrahigh-speed x-ray imaging. Science 363 (2019) 849–852. doi:10.1126/science.aav4687.

[18] M. Naderi, J. Weaver, D. Deisenroth, N. Iyyer, R. McCauley. On the fidelity of the scaling laws for melt pool depth analysis during laser powder bed fusion. Integr. Mater. Manuf. Innov. 12 (2023) 11–26. doi:10.1007/s40192-022-00289-w.

[19] A. M. Rubenchik, W. E. King, S. S. Wu. Scaling laws for the additive manufacturing. J. Mater. Process. Tech. 257 (2018) 234–243. doi:10.1016/j.jmatprotec.2018.02.034.

[20] D. B. Hann, J. Iammi, J. Folkes. A simple methodology for predicting laser-weld properties from material and laser parameters. J. Phys. D: Appl. Phys. 44 (2011) 445401. doi:10.1088/0022-3727/44/44/445401.

[21] K. N. Lankalapalli, J. F. Tu, M. Gartner. A model for estimating penetration depth of laser welding processes. J. Phys. D: Appl. Phys. 29 (1996) 1831–1841. doi:10.1088/0022-3727/29/7/018.

[22] S. I. Shahabad, U. Ali, Z. Zhang, A. Keshavarzkermani, R. Esmaeilizadeh, A. Bonakdar, E. Toyserkani. On the effect of thin-wall thickness on melt pool dimensions in laser powder-bed fusion of hastelloy x: Numerical modeling and experimental validation. J. Manuf. Processes 75 (2022) 435–449. doi:10.1016/j.jmapro.2022.01.029.

[23] S. Piazza, B. Merrigan, D. P. Dowling, M. Celikin. The effects of geometry and laser power on the porosity and melt pool formation in additively manufactured 316l stainless steel. J. Adv. Manuf. Technol. 111 (2020) 1457–1470. doi:10.1007/s00170-020-06196-8.

[24] K. Taherkhani, O. Ero, F. Liravi, S. Toorandaz, E. Toyserkani. On the application of in-situ monitoring systems and machine learning algorithms for developing quality assurance platforms in laser powder bed fusion: A review. J. Manuf. Processes 99 (2023) 848–897. doi:10.1016/j.jmapro.2023.05.048.

[25] U. Scipioni Bertoli, G. Guss, S. Wu, M. J. Matthews, J. M. Schoenung. In-situ characterization of laser-powder interaction and cooling rates through high-speed imaging of powder bed fusion additive manufacturing. Materials & Design 135 (2017) 385–396. doi:10.1016/j.matdes.2017.09.044.

[26] S. Ly, A. M. Rubenchik, S. A. Khairallah, G. Guss, M. J. Matthews. Metal vapor micro-jet controls material redistribution in laser powder bed fusion additive manufacturing. Sci. Rep. (2017). doi:10.1038/s41598-017-04237-z.

[27] P. Bidare, I. Bitharas, R. M. Ward, M. M. Attallah, A. J. Moore. Laser powder bed fusion in high-pressure atmospheres. J. Adv. Manuf. Technol. 99 (2018) 543–555. doi:10.1007/s00170-018-2495-7.

[28] P. Bidare, I. Bitharas, R. Ward, R. M. Ward, M. M. Attallah, A. J. Moore. Fluid and particle dynamics in laser powder bed fusion. Acta Mater. (2018). doi:10.1016/j.actamat.2017.09.051.

[29] A. A. Martin, J. Wang, P. J. DePond, M. Strantza, J.-B. Forien, J.-B. Forien, S. Gorgannejad, G. M. Guss, G. Guss, V. Thampy, A. Y. Fong, J. N. Weker, K. H. Stone, K. H. Stone, C. J. Tassone, M. J. Matthews, N. P. Calta. A laser powder bed fusion system for operando synchrotron x-ray imaging and correlative diagnostic experiments at the stanford synchrotron radiation lightsource. Rev. Sci. Instrum. (2022). doi:10.1063/5.0080724.

[30] B. Gould, S. Wolff, N. D. Parab, C. Zhao, M. C. Lorenzo-Martin, K. Fezzaa, A. Greco, T. Sun. In situ analysis of laser powder bed fusion using simultaneous high-speed infrared and x-ray imaging. JOM (2020). doi:10.1007/s11837-020-04291-5.

[31] A. A. Martin, N. P. Calta, J. A. Hammons, S. A. Khairallah, M. H. Nielsen, R. M. Shuttlesworth, N. Sinclair, M. J. Matthews, J. R. Jeffries, T. M. Willey, J. R. Lee. Ultrafast dynamics of laser-metal interactions in additive manufacturing alloys captured by in situ x-ray imaging. Mater. Today. Advances 1 (2019) 100002. doi:10.1016/j.mtadv.2019.01.001.

[32] B. J. Simonds, J. Tanner, A. Artusio-Glimpse, P. A. Williams, N. Parab, C. Zhao, T. Sun. Simultaneous high-speed x-ray transmission imaging and absolute dynamic absorptance measurements during high-power laser-metal processing. Procedia CIRP 94 (2020) 775–779. doi:10.1016/j.procir.2020.09.135.

[33] B. J. Simonds, J. Tanner, A. Artusio-Glimpse, P. A. Williams, N. Parab, C. Zhao, T. Sun. The causal relationship between melt pool geometry and energy absorption measured in real time during laser-based manufacturing. Appl. Mater. Today 23 (2021) 101049. doi:10.1016/j.apmt.2021.101049.

[34] S. A. Khairallah, T. Sun, B. J. Simonds. Onset of periodic oscillations as a precursor of a transition to pore-generating turbulence in laser melting. Addit. Manuf. Letters 1 (2021) 100002. doi:10.1016/j.addlet.2021.100002.

[35] S. A. Khairallah, A. A. Martin, J. R. I. Lee, G. Guss, N. P. Calta, J. A. Hammons, M. H. Nielsen, K. Chaput, E. Schwalbach, M. N. Shah, M. G. Chapman, T. M. Willey, A. M. Rubenchik, A. T. Anderson, Y. M. Wang, M. J. Matthews, W. E. King. Controlling interdependent meso-nanosecond dynamics and defect generation in metal 3d printing. Science 368 (2020) 660–665. doi:10.1126/science.aay7830.

[36] B. Lane, I. Zhirnov, S. Mekhontsev, S. Grantham, R. Ricker, S. Rauniyar, K. Chou. Transient laser energy absorption, co-axial melt pool monitoring, and relationship to melt pool morphology. Addit. Manuf. 36 (2020). doi:10.1016/j.addma.2020.101504.

[37] C. K. P. Vallabh, S. Sridar, W. Xiong, X. Zhao. Predicting melt pool depth and grain length using multiple signatures from in-situ single camera two-wavelength imaging pyrometry for laser powder bed fusion. J. Mater. Process. Tech. 308 (2022) 117724. doi:10.1016/j.jmatprotec.2022.117724.

[38] M. P. Haines, N. J. Peter, S. S. Babu, E. A. Jägle. In-situ synthesis of oxides by reactive process atmospheres during l-pbf of stainless steel. Addit. Manuf. 33 (2020) 101178. doi:10.1016/j.addma.2020.101178.

[39] V. Renken, A. von Freyberg, K. Schünemann, F. Pastors, A. Fischer. In-process closed-loop control for stabilising the melt pool temperature in selective laser melting. Prog. Addit. Manuf. 4 (2019) 411–421. doi:10.1007/s40964-019-00083-9.

[40] Aconity Control, Aconity 3D, 2024.

[41] J. Trapp, A. M. Rubenchik, G. Guss, M. J. Matthews. In situ absorptivity measurements of metallic powders during laser powder-bed fusion additive manufacturing. Appl. Mater. Today 9 (2017) 341–349. doi:10.1016/j.apmt.2017.08.006.

[42] M. Leitner, G. Pottlacher. Density of liquid niobium and tungsten and the estimation of critical point data. Metall. Mater. Trans. A 50 (2019) 3646–3653. doi:10.1007/s11661-019-05262-5.

[43] V. Y. Bodryakov. Correlation of temperature dependences of thermal expansion and heat capacity of refractory metal up to the melting point: Tungsten. High Temp. 53 (2015) 643–648. doi:10.1134/s0018151x15040069.

[44] J. G. Hust, L. A. B. Thermal conductivity of aluminum, copper, iron, and tungsten for temperatures from 1 k to the melting point: Nbsir 84-3007 (1984).

[45] I. Bitharas, N. Parab, C. Zhao, T. Sun, A. D. Rollett, A. J. Moore. The interplay between vapour, liquid, and solid phases in laser powder bed fusion. Nat. Commun. 13 (2022) 2959. doi:10.1038/s41467-022-30667-z.

[46] G. Petzow, Metallographic etching, American Soc. for Metals, Metals Park, Ohio, 1978.

[47] C. A. Schneider, W. S. Rasband, K. W. Eliceiri. Nih image to imagej: 25 years of image analysis. Nat. Methods 9 (2012) 671–675. doi:10.1038/nmeth.2089.

[48] F. Pedregosa, G. Varoquaux, A. Gramfort, V. Michel, B. Thirion, O. Grisel, M. Blondel, P. Prettenhofer, R. Weiss, V. Dubourg, et al. Scikit-learn: Machine learning in python. JMLR 12 (2011) 2825–2830.

[49] W. E. King, H. D. Barth, V. M. Castillo, G. F. Gallegos, J. W. Gibbs, D. E. Hahn, C. Kamath, A. M. Rubenchik. Observation of keyhole-mode laser melting in laser powder-bed fusion additive manufacturing. J. Mater. Process. Tech. 214 (2014) 2915–2925. doi:10.1016/j.jmatprotec.2014.06.005.

[50] J. A. Mitchell, T. A. Ivanoff, D. J. Dagel, J. D. Madison, B. H. Jared. Linking pyrometry to porosity in additively manufactured metals. Addit. Manuf. (2020). doi:10.1016/j.addma.2019.100946.

[51] K. Ettaieb, S. Lavernhe, C. Tournier. A flash-based thermal simulation of scanning paths in lpbf additive manufacturing. Rapid Prototyping J. 27 (2021) 720–734. doi:10.1108/RPJ-04-2020-0086.

[52] C. Wang, Z. J. Li, C. Q. Ji, S. W. Gao, Y. N. Cui. Crystal plasticity analysis of the evolutions of temperature, stress and dislocation in additively manufactured tungsten. Int. J. Refract. Met. Hard Mater 110 (2023) 106041. doi:10.1016/j.ijrmhm.2022.106041.

[53] R. Fabbro. Depth dependence and keyhole stability at threshold, for different laser welding regimes. Appl. Sci. 10 (2020) 1487. doi:10.3390/app10041487.

[54] X. Xiao, X. Liu, M. Cheng, L. Song. Towards monitoring laser welding process via a coaxial pyrometer. J. Mater. Process. Tech. 277 (2020) 116409. doi:10.1016/j.jmatprotec.2019.116409.

[55] P. F. Goldsmith, Quasioptical systems, IEEE Xplore Digital Library, IEEE Press, Piscataway NJ, 1998. Restricted to subscribers or individual electronic text purchasers.